PNAS RESEARCH ARTICLE | PHYSICS

Identifying microscopic factors that influence ductility in disordered solids

Hongyi Xiao[a,b,c,1], Ge Zhang[a,d,1], Entao Yang[e,1], Robert Ivancic[f,1], Sean Ridout[a,g], Robert Riggleman[e], Douglas J. Durian[a,h], and Andrea J. Liu[a,h,2]

Edited by Michael Cates, University of Cambridge, Cambridge, United Kingdom; received May 9, 2023; accepted August 16, 2023

There are empirical strategies for tuning the degree of strain localization in disordered solids, but they are system-specific and no theoretical framework explains their effectiveness or limitations. Here, we study three model disordered solids: a simulated atomic glass, an experimental granular packing, and a simulated polymer glass. We tune each system using a different strategy to exhibit two different degrees of strain localization. In tandem, we construct structuro-elastoplastic (StEP) models, which reduce descriptions of the systems to a few microscopic features that control strain localization, using a machine learning-based descriptor, softness, to represent the stability of the disordered local structure. The models are based on calculated correlations of softness and rearrangements. Without additional parameters, the models exhibit semiquantitative agreement with observed stress–strain curves and softness statistics for all systems studied. Moreover, the StEP models reveal that initial structure, the near-field effect of rearrangements on local structure, and rearrangement size, respectively, are responsible for the changes in ductility observed in the three systems. Thus, StEP models provide microscopic understanding of how strain localization depends on the interplay of structure, plasticity, and elasticity.

disordered solids | brittle-to-ductile transition | shear band | machine learning

Significance

Disordered solids are ubiquitous, with many useful mechanical, thermal, and optical properties, but differ in their responses to large deformations. While shaving cream is ductile, able to deform indefinitely, many disordered solids, such as window glass, are brittle. This limits applications. Empirical research has uncovered ways to improve ductility but offers little insight into their success or how to generalize to new materials. Here, we study three very different systems whose ductility is tuned differently. Previous theoretical approaches focused on interactions between plasticity with elasticity. To go further, we construct models that incorporate structure into this interplay. Our theory captures behaviors we observe experimentally and by computer simulations and yields insight into microscopic mechanisms underlying empirical strategies for tuning ductility.

All solids yield under sufficiently high mechanical loads. Below yield, the mechanical responses of all disordered solids are nearly alike (1), but above yield, every different disordered solid responds in its own way (2–5). Brittle systems can shatter without warning, like ordinary window glass, or exhibit strain localization prior to fracture, like metallic or polymeric glasses. Ductile systems, e.g., foams like shaving cream or emulsions like mayonnaise, can deform indefinitely with no strain localization.

Several empirical strategies have been discovered for tuning strain localization. Reducing the range of interparticle attractions (6–10), equilibrating better (11), annealing at slower cooling rates (12), or cooling while loading (8, 13) all enhance strain localization. Friction (14), composite constituents (15), particle shape (16), and degree of crystallinity (7) also influence ductility. However, we do not understand why or how these factors influence strain localization. For each new system, it is also not clear which if any of these strategies will prove useful for improving ductility.

At the microscopic scale, plasticity in solids is produced by rearrangements in which constituent particles change neighbors. While other approaches exist (17–20), elastoplasticity (EP) models (21) update and record yield strain and strain at each lattice site, corresponding to a coarse-grained region. Such models typically assume an underlying distribution of local yield strains that controls the degree of strain localization (22) and is put in by hand (5, 21).

Here, we follow a different path. A particle's local yield strain—and hence its probability to rearrange—depends on its local structural environment (23–26). We extract a structural predictor of local yield strain, called softness, S (27, 28), using neural networks or support-vector machines, demonstrating that our framework can use any local structural measure that predicts rearrangements or local yield stress, e.g., refs. 29–36. Following Zhang et al. (37, 38), we unravel the interplay between strain, rearrangements, and softness, to incorporate softness into structuro-elastoplastic (StEP) models.

We develop StEP models for three vastly different systems, each of which is tuned in a different way to exhibit a varying degree of strain localization. System I is a simulated two-dimensional (2D) system of repulsive polydisperse circular disks, prepared at an initial temperature T_a using Monte Carlo swap methods (11), quenched to $T = 0$ and then sheared quasistatically. System IA is equilibrated at high T_a and is ductile, while IB is equilibrated at very low T_a and is brittle (11). System II is an experimental granular raft, a 2D monolayer of polydisperse spheres floating at an air-oil interface (9). The gravitational capillary length ℓ_c controls the attractive interaction range between nearby

Author contributions: R.R., D.J.D., and A.J.L. designed research; H.X., G.Z., E.Y., and R.I. performed research; H.X., G.Z., E.Y., R.I., and S.R. analyzed data; and H.X., G.Z., E.Y., R.I., S.R., R.R., D.J.D., and A.J.L. wrote the paper.

The authors declare no competing interest.

This article is a PNAS Direct Submission.

[1]H.X., G.Z., E.Y., and R.I. contributed equally to this work.

[2]To whom correspondence may be addressed. Email: ajliu@physics.upenn.edu.

This article contains supporting information online at https://www.pnas.org/lookup/suppl/doi:10.1073/pnas.2307552120/-/DCSupplemental.

Published October 9, 2023.

particles. In the more ductile System IIA, ℓ_c exceeds the mean diameter, d, while in the more brittle IIB, $\ell_c < d$. Finally, System III is a three-dimensional (3D) cylindrical polymer nanopillar of chains of coarse-grained particles below the glass transition temperature (8, 39). Monomers in the same chain are bonded by a stiff harmonic potential, while the nonbonded monomer interaction is a modified Lennard-Jones potential. System IIIA is simulated at a higher temperature, T, and is more ductile, while the lower-T System IIIB exhibits more strain localization. For details of all three systems, *Materials and Methods*. We demonstrate that StEP models can be used to identify the microscopic factors that determine ductility in each case, opening the door to quantitative, particle-level approaches to engineer advanced structure-property relations in disordered solids.

Structuro-elastoplastic Models

We extend the recently developed 2D athermal StEP framework (37), implemented in a 2D model in ref. 38 to the 2D and 3D lattice models depicted in Fig. 1. Each lattice site stores the local elastic strain, $\tilde{\epsilon}_i$, and softness, S_i. The initial softness field is assigned from a Gaussian distribution (38),

$$P(S) = \frac{1}{\sigma_S\sqrt{2\pi}} e^{-\frac{1}{2}\left(\frac{S-\langle S\rangle}{\sigma_S}\right)^2}, \qquad [1]$$

with the mean, $\langle S\rangle$, and the SD, σ_S, matching that of the corresponding particle-based system. The StEP model then predicts the evolution of the elastic strain field, rearrangement events, and the softness field upon deformation.

The driving global strain, ϵ_G, is uniformly added to all blocks at each time step as simple shear (System I) or tensile strain (Systems II and III), resulting in the accumulation of $\tilde{\epsilon}_i$. Block i undergoes a plastic event if $|\tilde{\epsilon}_i| > \epsilon_{Y,i}$, which releases its elastic strain and induces a long-range strain field through an elastic kernel that connects the neighboring sites (40, 41). The kernel is similar to the one commonly used (41) but includes more strain components (37), as detailed in supporting information (42). For the rearranging block i itself, the elastic strain is converted to plastic strain $\tilde{\epsilon}_p$. We neglect variation of local elastic constants so stress is proportional to elastic strain.

Particles with higher softness tend to have lower yield strains and are therefore more susceptible to rearrangement (*SI Appendix*, Fig. S1). The local yield strain of site i, $\epsilon_{Y,i}$, is randomly drawn from a distribution with parameters that depend on the site's softness S_i, which is Gaussian for System I and Weibull for Systems II and III (*Materials and Methods*):

$$\text{System I}: \; P(\epsilon_Y, S) = \frac{1}{\sigma_{\text{YS}}\sqrt{2\pi}} e^{-\frac{1}{2}\left(\frac{\epsilon_Y-\langle\epsilon_Y\rangle}{\sigma_{\text{YS}}}\right)^2}$$

$$\text{Systems II \& III}: \; P(\epsilon_Y, S) = \frac{k}{\lambda}\left(\frac{\epsilon_Y}{\lambda}\right)^{k-1} e^{(\epsilon_Y/\lambda)^k}, \qquad [2]$$

where $\langle\epsilon_Y\rangle(S)$ and σ_{YS} characterize the Gaussian and k and $\lambda(S)$ characterize the Weibull distribution at each softness S (*SI Appendix*, Figs. S3–S5). The two Weibull parameters, k and

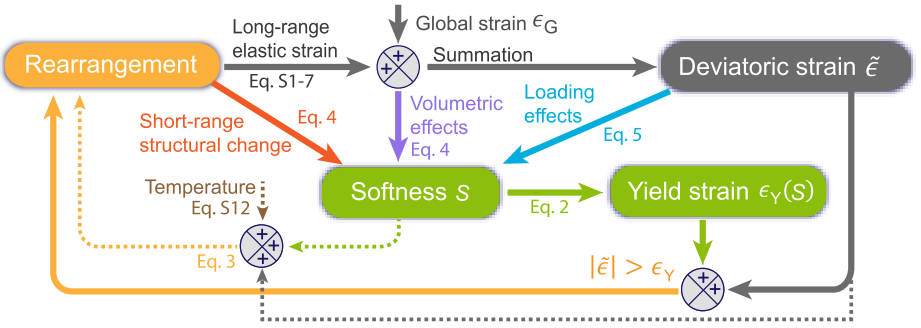

Parameter	Eq.#	System IA	System IB	System IIA	System IIB	System IIIA	System IIIB
$\langle S\rangle$	[1]	0.00	-2.73	-0.09	-0.04	0.575	0.085
σ_S	[1]	3.18	2.28	0.78	0.70	0.70	0.72
$\langle\epsilon_Y\rangle(S)$	[2]	$(12.09-S)/89$	$(12.09-S)/89$	$0.013-0.0006S$	$0.012-0.00245S$	$\max(0.0484$ $-0.102S, 0.0382)$	$0.0484-0.0045S$
$\epsilon_Y(S)$ distribution	[2]	$\sigma_{\text{YS}}=3.08$	$\sigma_{\text{YS}}=2.20$	$k=1.9$	$k=2.1$	$k=2.02$	$k=1.84$
$C_{th}(T)$	[3]	–	–	–	–	$T=0.05$	$T=0.30$
$\eta(r)$	[4]	$0.078r^{-2.5}$	$0.078r^{-2.5}$	$0.1e^{-r/1.4}$	$0.09e^{-r/0.65}$	$0.206e^{-r/1.02}$ $+0.059$	$0.162e^{-r/1.45}$ $+0.011$
c	[4]	-3.25	-3.25	0.08	1.20	0	0
ζ	[4]	244	226	2.37	1.74	9.17	16.60
κ	[5]	411	411	139	339	13.50	11.05
C_{d2min}	[6]	$1.0e^{-r/1.88}$	$1.0e^{-r/1.63}$	$1.0e^{-r/1.13}$	$1.0e^{-r/1.12}$	$1.40e^{-r/0.75}$	$0.87e^{-r/1.11}$

Fig. 1. Schematic and parameters of the StEP model. A strain release (plastic rearrangement event) at a given block changes the softness of nearby blocks, and elastically propagates a long-ranged deviatoric strain field. Softness determines the yield strain for each block. A new rearrangement is triggered if the deviatoric strain exceeds the yield strain. In thermal systems, rearrangements can also be triggered by thermal fluctuations; (*SI Appendix*, Fig. S14). Structural/elastic/plastic/thermal components of the model are in green/gray/orange/brown, respectively. Each arrow represents an independently determined equation, and corresponding parameters are shown in the table with matching colors. Key parameters for triggering the ductile-to-brittle transition are highlighted in white and are different for each system. The corresponding equations are referenced by the numbers next to the variables.

λ, are related to the mean and variance of the distribution and depend on S. We record the percentile of the random number in the distribution and only reassign it upon a plastic event at the site. Note that in the absence of a plastic event, $\epsilon_{Y,i}$ still evolves when S_i and the corresponding $\epsilon_{Y,i}$ distribution change, even though the percentile remains the same (38).

For System III at nonzero temperature T, we allow rearrangements to be triggered also by thermal fluctuations with a softness-dependent probability, C_{th}, given by

$$C_{th}(S, |\tilde{\epsilon}|, \epsilon_Y, T) = \exp(-\Delta F(S) \cdot (1 - |\tilde{\epsilon}|^2/\epsilon_Y^2)/T), \quad [3]$$

where $\Delta F(S, T)$ is a softness-dependent free energy barrier for rearrangements in a quiescent system, $|\tilde{\epsilon}|$ is the strain magnitude at the lattice site, and ϵ_Y is the yield strain for the site. This expression for the probability is derived in ref. 42.

As the StEP models include not only coupling between plasticity and elasticity, but also with structure, a rearrangement at site i affects other sites j via not only an elastic but also a softness kernel consisting of two main pieces. The first contribution, $\Delta S_{\rm n}$, is a near-field effect from the change of local structure near a rearrangement, which alters softness of nearby particles directly. For all three systems, we find that this contribution tends to restore S to a value close to the local angular-averaged softness, as in ref. 37. The far-field term, $\Delta S_{\rm f}$, arises from treating a rearrangement as an Eshelby inclusion that exerts a far-field strain (40, 43, 44). This "elastic facilitation" distorts local structural environments via the volumetric strain, $\tilde{\epsilon}_{\rm vol}$ (37, 38). Fluctuations around this average behavior are approximated with a Gaussian noise term, $\delta(r)$. Altogether, the softness kernel at distance r from a rearrangement is

$$\Delta S(r, S) = \underbrace{\eta(r)(\langle S\rangle + c - S) + c' + \delta(r)}_{\Delta S_{\rm n}} + \underbrace{\zeta\tilde{\epsilon}_{\rm vol}}_{\Delta S_{\rm f}}, \quad [4]$$

where the parameters η, c, and ζ are measured from the corresponding simulations or experiments for each of our systems (42). Here, c' is a lattice artifact defined as the average of $-c\langle\eta(r)\rangle$ over all sites. This term allows the average softness to reach a constant value at steady state for a volume-conserving shear deformation (38) and vanishes in the continuum limit. These parameters are extracted from the particle simulations or experiments [*SI Appendix*, Figs. S6–S8 (42)]. The noise term has a Gaussian distribution (*SI Appendix*, Figs. S9–S11) with a variance determined as $\eta(r)[2 - \eta(r)]\sigma_S^2$, which can maintain a constant softness distribution in steady state (38).

Furthermore, we account for the effect that the uniform deviatoric strain also deforms local structural environments (1) and therefore it changes S_i by

$$\Delta S_{\rm load} = \kappa\Delta|\tilde{\epsilon}|^2, \quad [5]$$

where $\Delta|\tilde{\epsilon}|^2$ is the increment of $\tilde{\epsilon}_{\alpha\beta}\tilde{\epsilon}_{\beta\alpha}$ in each strain step (38). As a consequence, the average softness of the system increases upon loading, which lowers the barriers to rearrangement per previous observations (27, 45).

In standard elasto-plastic (EP) models, the lattice size is the rearrangement size, but the softness kernel in Eq. **4** uses r in units of particle diameter. To avoid rescaling the kernel, rearrangements in the StEP model span several blocks (38). The rearrangement size is characterized by the decay length, ξ, of the correlation function of particle nonaffine displacement (19), C_{d2min}, measured for Systems I-III (42), and blocks at distance r from the rearranging block release their elastic strain with a probability,

$$C(r) \propto \exp(-r/\xi), \quad [6]$$

which is shown in *SI Appendix*, Figs. S12–S13 (42) with measurements from the particle systems.

In summary, the predicted response to strain emerges from the interplay between elasticity, plasticity, and structure. The parameters that characterize the interplay are measured directly from simulations and experiments and listed in Fig. 1. We stress that there are no additional fitting parameters in the StEP model. Note that the parameters of the A and B configurations may be directly compared, as we do below under Elucidating mechanisms, since the parameter extraction procedures are exactly the same.

Results

StEP Models Predict the Ductile-to-Brittle Transition. Our model successfully produces at least qualitative agreement with both cases of all three particle systems. We demonstrate the qualitative deformation behavior in Fig. 2 and quantitative measurements in Fig. 3. In Fig. 2, the spatial distribution of accumulated plasticity is shown for examples of the A and B configurations of the three model systems. In the particle systems, plasticity is quantified by the nonaffine displacement $D^2_{\rm min}$ (19), in units of d^2, during a small applied strain interval $\Delta\epsilon_G$. In the StEP models, it is the magnitude of the plastic strain $|\tilde{\epsilon}_p|$ accumulated during the same strain interval. For each system, the spatial distribution of plasticity is shown at three different applied global strains ϵ_G for the particle realization (*Top* row) and the corresponding StEP predictions (*Bottom* row). Note that the StEP model is not designed to reproduce the actual spatial distribution of plasticity but only its statistical features. Nevertheless, the difference in strain localization between cases A and B is captured well by the StEP models: For the more ductile cases (A) displayed on the *Left* part of Fig. 2, the plasticity is distributed throughout the spatial domain, while for the less ductile cases (B) on the *Right*, a clear and long-lasting shear band develops at large ϵ_G.

For soft repulsive disks quenched from $T_a = 0.2$ to $T = 0$, (System IA), there is no strain localization and the stress–strain curve shows a smooth yielding process with no stress drops in both StEP-model and particle simulations (Fig. 3*A*). Spatially correlated rearrangements appear at larger ϵ_G, but there is no system-spanning shear band. For the well-annealed (11, 18, 22) case quenched from $T_a = 0.025$ to $T = 0$ (IB), the StEP model captures the sharp shear band that emerges at higher strain, along with the accompanying stress drop (Fig. 3*A*). Features in the stress–strain curves and the softness statistics (Fig. 3 *A* and *D*) are captured reasonably well by the StEP models, although the StEP models yield at a lower strain than the particle simulations in the brittle case and the stress drop is smaller.

For the experimental granular raft pillars (System II) in the elastic regime ($\epsilon_G = 0.1\%$), small plastic events are distributed throughout in both the StEP model and the experiment for Systems IIA and IIB. As ϵ_G increases to 0.8%, transient shear bands at 45° to the principal extension direction are apparent in both the StEP model and experiment. At $\epsilon_G = 2.5\%$, system-spanning shear bands appear in both pillars but with a different morphology. For System IIA, where the particle interaction range exceeds the particle size, the shear bands contain rather sparse rearrangements and are transient in the StEP model; in the experiment, the shear bands are locked in the same location due to

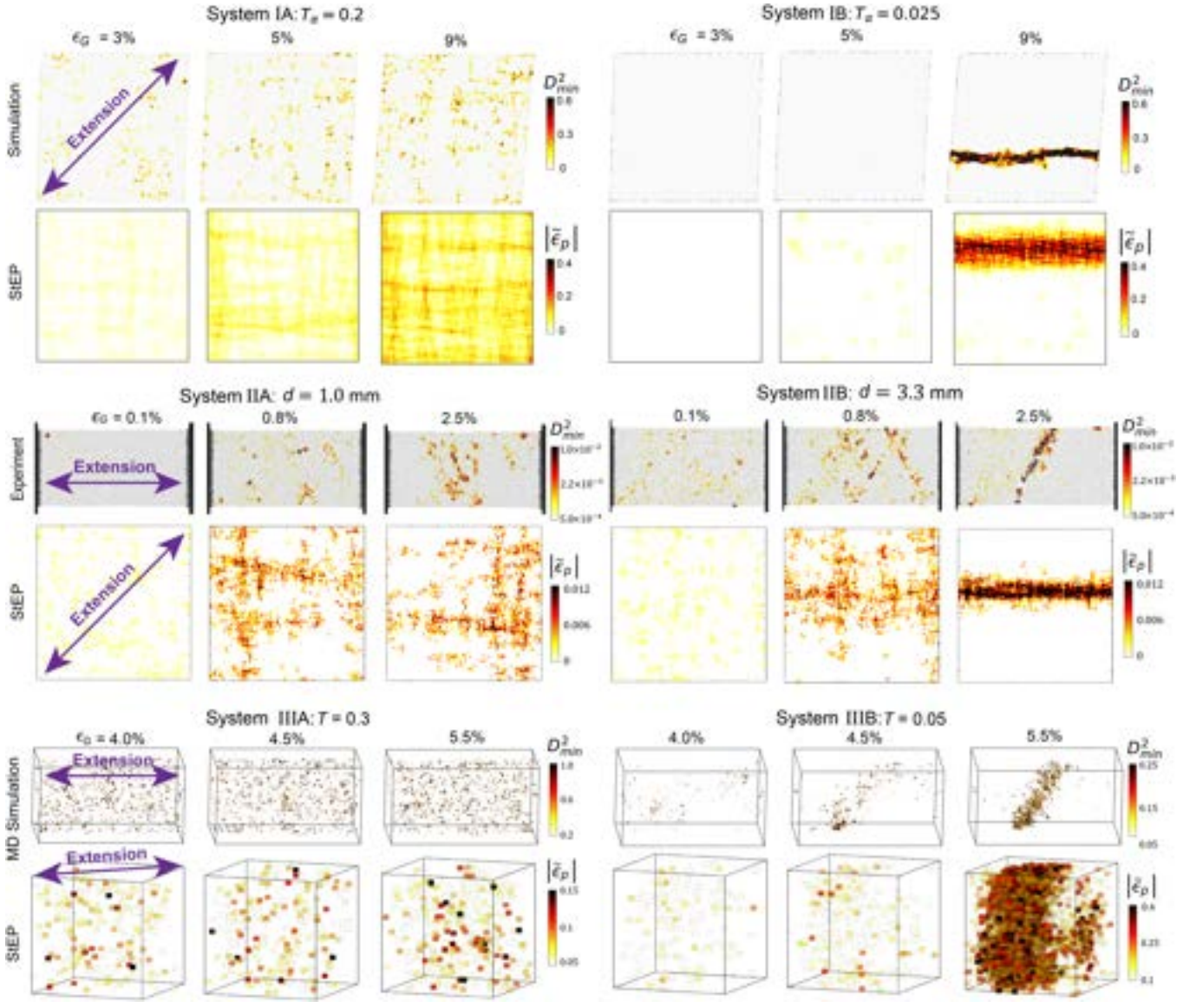

Fig. 2. Comparison of spatial plasticity field for particle results and StEP models. Each column shows the plasticity fields at a different global shear strain ϵ_G. For each system, the first row shows the particle simulation/experiment result, and the second row shows the StEP results. System I consists of N polydisperse disks at density $\rho = 1$ with $1/r_d^{12}$ pairwise repulsion, where r_d is the separation (11). System IA has N = 64,000 disks initially equilibrated at $T_a = 0.2$, while System IB has N = 10,000 disks initially equilibrated at $T_a = 0.025$, before rapid quenching to $T = 0$. The corresponding StEP models are computed on a $L \times L$ grid, with $L = 253 \approx \sqrt{N}$ for System IA and $L = 100 = \sqrt{N}$ for System IB. System II consists of $120\,d \times 60d$ granular rafts of polydisperse Styrofoam spheres of mean diameter $d = 1.0 \pm 0.1$ mm (System IIA) and $d = 3.3 \pm 0.3$ mm (System IIB), respectively. The spheres float on an air-oil interface and the rafts are subjected to quasistatic extension as indicated. The corresponding StEP models are computed on a 120 × 120 grid. System III consists of polymer nanopillars made of $\approx 4 \times 10^4$ bead-spring polymers, with 5 monomers per chain at temperature $T = 0.30$ for System IIIA and $T = 0.05$ for System IIIB. Each pillar is a cylinder with a length of 100 bead diameters with periodic boundary conditions and radius of 25 bead diameters. The corresponding StEP models are computed on a 21 × 21 × 21 grid in units of bead diameter.

necking of the pillar. For System IIB, where the interaction range is smaller than the particle size, the shear band is sharper with much more concentrated rearrangements than IIA, indicating greater strain localization. The shear band location is fixed in both StEP model and experiment. The stress–strain curves, and the evolution of the mean and SD of S with ϵ_G are captured well by the StEP models (Fig. 3 *B* and *E*). The one exception is the SD of softness after the long-lasting shear band forms in System IIB, as expected since S is not trained for large fractures in the particle packing.

For the thermal 3D polymer nanopillar systems (last 2 rows of Fig. 2), the StEP model also captures qualitative behavior. At large ϵ_G, isolated rearrangements are seen for System IIIA at $T = 0.3$, while strain localization and shear banding occur for System IIIB at $T = 0.05$ for both the StEP model and simulations. Quantitative comparisons (Fig. 3 *C* and *F*) show that stress reaches a higher value in the StEP model.

Systems I-III differ in the size of the constituent particles (and hence importance of temperature), interparticle interactions, system dimension, importance of friction, and preparation history. Yet in all 6 cases, StEP models describe them semiquantitatively, indicating that they capture the salient microscopic differences in the interplay between elasticity, plasticity, and the disordered structure.

Elucidating Microscopic Mechanisms Controlling Ductility. Although preparation history, interaction range and temperature are known to affect strain localization, it is not understood why

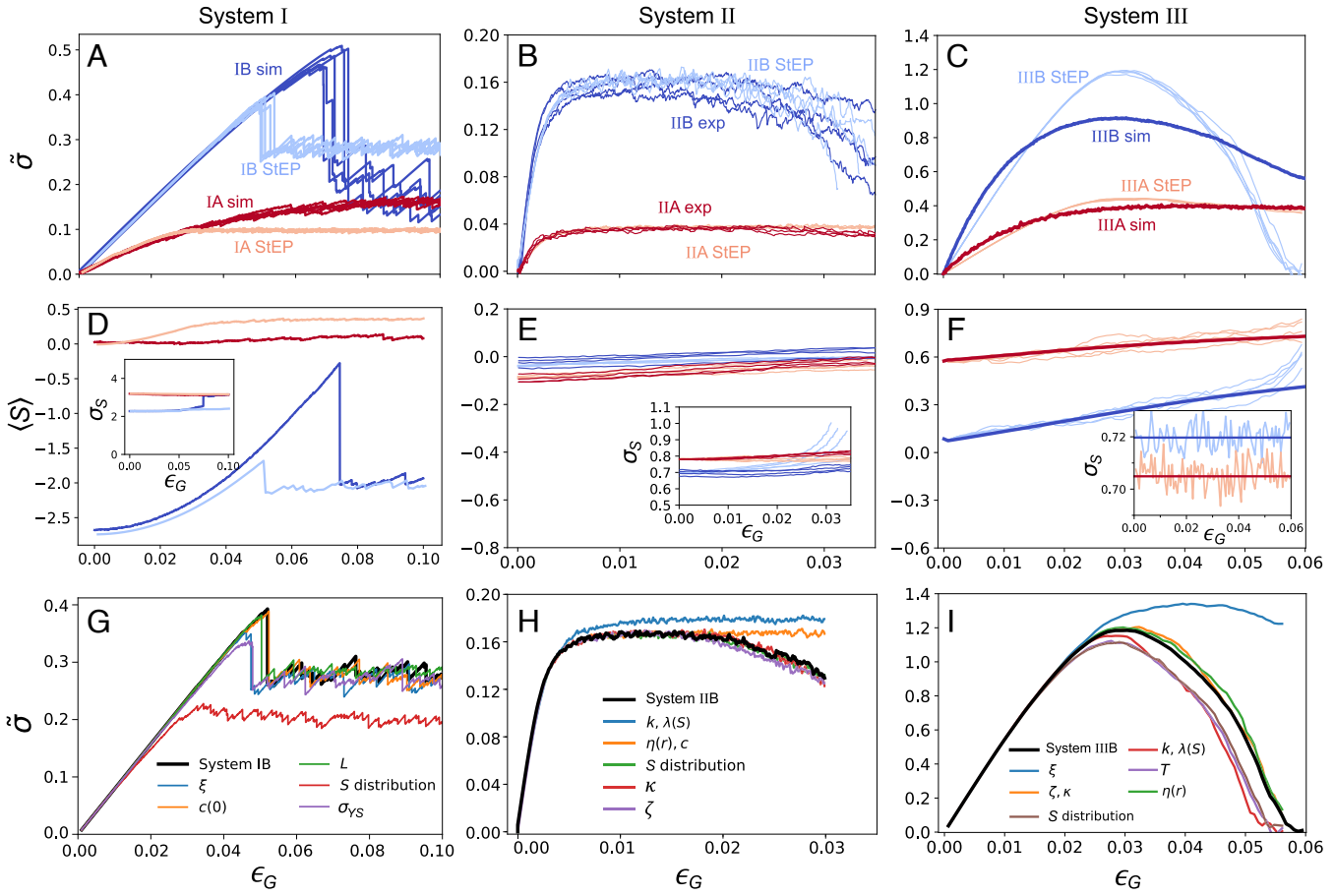

Fig. 3. Quantitative comparison between particle simulation/experiment results and StEP models. Cases (I-III)A are denoted by red curves and cases (I-III)B by blue curves. Darker shades correspond to the simulations/experiments while lighter shades correspond to the StEP model. First row (*A–C*): Stress–strain curves; stress is calculated as the product of elastic strain modulus summed over all sites and global modulus measured in the corresponding system. Second row (*D–F*): Average softness vs. strain; insets show SD of the softness distribution vs. strain. In *G–I*, the stress–strain curve for the StEP models for Case B is shown as a thick solid black line. For each microscopic factor characterizing the StEP models, the corresponding parameters in Fig. 1 were varied from their values for Case B to those for Case A.

they are important. StEP models allow us to gain insight by transmuting these factors in the particle systems into factors in the StEP framework such as the softness distribution and softness kernel. By exploring how these factors vary between the A and B variations of each system, we can gain insight into the underlying microscopic mechanisms controlling ductility—we can determine how controllable properties such as interaction range affect the interplay of structure, elasticity, and plasticity.

For System I, the table in Fig. 1 shows that Eq. **4** is identical for IA and IB. The only striking difference is in the initial mean softness, $\langle S \rangle$. The initial SD of the softness distribution, the relation between S_i and the yield strain $\epsilon_{Y,i}$, and the size of rearrangements are also slightly different. To determine the significance of each of these factors, we start with System IB (bold black curve in Fig. 3*G*) and systematically vary each of these parameters (colored curves) one at a time from its value in IB (brittle) to its value in IA (ductile) and assess the effect on the stress–strain curve to see which parameter has the strongest influence. Fig. 3*G* shows that the only factor that qualitatively affects the stress–strain curve is the initial distribution of S. Switching the initial S distribution to its value in the ductile case of System IA removes the large stress drop in the stress–strain curve. Thus, the only significant difference between Systems IA and IB is the initial S_i distribution. This makes sense; Systems IA and IB are prepared differently, which affects the initial S distribution. Brittle systems obtained by annealing at lower T_a are more stable (11, 46, 47), leading to lower S and higher values of local yield strain. Thus, extracting StEP models from particle-level data leads to the correct identification of the microscopic factors controlling strain localization.

For the granular pillars, System II, the values of nearly all of the parameters differ from System IIA to IIB. However, by changing them individually (Fig. 3*H*) from their values for System IIB (bold black curve) to those for System IIA, we can see that only two sets of parameters make a significant difference to the stress–strain curve. One can flatten the curve by reducing the dependence of the yield strain on softness, characterized by the Weibull exponent k and mode $\lambda(S)$. The near-field ΔS caused by rearrangement, i.e., the first term in Eq. **4**, is also important. This near-field effect is characterized by the range $\eta(r)$ and offset c. System IIA has a larger decay length of $\eta(r)$ and a smaller c. In other words, rearrangements in System IIB, which has a shorter particle interaction range, alter local yield strain more strongly over a shorter distance. The range of the near-field ΔS is comparable to the interaction range.

The values of most of the parameters for the polymer nanopillar StEP models differ from System IIIA to IIIB (table in Fig. 1), but we change them one-by-one from their values for System IIIB to their values for System IIIA in Fig. 3*I*. The only parameter to affect the stress–strain curve appreciably is the rearrangement size, ξ. Rearrangements in the low-temperature system, System IIIB,

are larger, allowing for more facilitation and thus leading to stronger strain localization.

Discussion

For three systems, we have shown that StEP models provide physical insight into the microscopic mechanisms governing ductility. The systems were chosen to be very different, and the microscopic mechanisms underlying the degree of strain localization turn out to be different. For simulated glasses with different preparation histories, we find that it is the initial distribution of softness, and hence of local yield stress, that controls ductility. For experimental granular pillars with different interaction ranges, it is the sensitivity of local yield strain to local structure and the near-field change of softness due to rearrangements that change, with a larger change of local yield stress over a shorter distance in systems with higher strain localization. Finally, for the simulated polymer glass nanopillars, we find that the rearrangement size is larger in cooler systems, allowing for more facilitation and leading to greater strain localization. This work focuses on identifying the aspects of the interplay among structure, elasticity, and plasticity that control strain localization, opening the door to studies of the detailed microscopic mechanisms that link experimentally controllable factors (e.g., the particle interaction range) to the interplay (e.g., the sensitivity of local yield strain to softness). This line of research raises the possibility that StEP models could be used to help design materials with desired ductility by optimizing over multiple controllable factors. This would be a substantial improvement over empirical approaches. This hope does not seem unrealistic; softness has been proven to be highly predictive of rearrangements in a wide range of disordered solids (1, 48). Moreover, the StEP model framework is highly adaptable, accommodating any structural predictor of rearrangements, as we have shown by introducing a structural predictor of local yield stress obtained using image classification methods instead of the more standard predictor of rearrangements (28).

For possible future directions, it is straightforward to extend StEP models to finite strain rate by using time-dependent softness and elastic kernels (24) to capture rheology. Like EP models, StEP models can also readily be extended to include local elastic moduli and other effects (21).

Materials and Methods

System I: Soft Repulsive Disks. This computer-simulated 2D soft-disk system is polydisperse (49). Disks interact via $1/r_d^{12}$ pairwise repulsions, where r_d is the separation, and samples are prepared using swap Monte-Carlo methods (49). System IA is equilibrated at $T_a = 0.2$, while for IB $T_a = 0.025$. Initial states for IB may not be completely equilibrated, but this does not affect interpretation of the results. After energy minimization to $T = 0$, these configurations are sheared athermally and quasistatically by repeatedly applying a small simple shear strain of $\delta\epsilon = 10^{-5}$ and minimizing the potential energy, up to total strain $\epsilon_{\text{end}} = 0.1$. Energy minimization is carried out using the steepest descent algorithm with a very conservative step size to simulate overdamped dynamics (*SI Appendix* in ref. 37). During minimization, we study intermediate configurations using the same protocol as ref. 37 to investigate the course of an avalanche.

System II: Granular Rafts. Each raft is a disordered monolayer of polydisperse granular particles of rectangular shape, floating at an air-oil interface (9). Mineral oil was used with density $\rho_{\text{oil}} = 870 \pm 10$ kg/m^3; the Styrofoam particles have density 15 kg/m^3. Systems IIA and IIB have different particle size distributions, with average particle sizes of 1.0 ± 0.1 mm for IIA and 3.3 ± 0.3 mm for IIB. Capillary attractions exist between nearby particles, with characteristic interaction range set by the capillary length, $l_c = \sqrt{\gamma_{\text{oil}}/\rho_{\text{oil}}g} = 1.8$ mm, where $\gamma_{\text{oil}} = 27.4$ dyn cm^{-1}, and $g = 9.8$ m/s^2 (9). Quasistatic tensile tests with strain rate on the order of 10^{-5} s^{-1} were conducted, and all particle positions and global tensile force were tracked throughout for 50 experiments (9) on $80d \times 40d$-sized pillars for each system to construct the StEP models. For comparing with StEP models, results from 12 experiments of larger pillars ($120d \times 60d$) were used for better statistics.

System III: Polymer Nanopillars. Using LAMMPS, we simulate bead-spring polymer nanopillars with $N = 5$ monomers per chain (39). We bond monomers using a stiff harmonic potential $U^b_{i,j} = \frac{k}{2}\left(r_{i,j} - d\right)^2$, where $r_{i,j}$ is the distance between monomers i and j and $k = 2,000\epsilon_{\text{LJ}}/d$ with ϵ_{LJ} being the dispersion energy. Nonbonded interactions are a modified Lennard-Jones potential $U^{nb}_{i,j} = 4\epsilon_{\text{LJ}}\left(\left(\frac{d'}{r_{i,j}-\Delta}\right)^{12} - \left(\frac{d'}{r_{i,j}-\Delta}\right)^{6}\right)$ where $d' = (1 - 3/2^{13/6})d$, $\Delta = 3d/4$. This modification increases the curvature while maintaining the minimum at $r_{\text{min}} = 2^{1/6}d$, causing more strain localization (8). For all simulations, we use a timestep of 6.64×10^{-4}. We thermalize our simulations within a cylindrical, harmonic confining wall at $T = 0.5$, that we fix to ensure the density of the monomers within the wall is $\rho = 0.3$. We then cool our simulation at a rate of 5×10^{-4} past the glass transition temperature of $T_g \approx 0.38$ to $T = 0.30$ (Systems IIIA) and $T = 0.05$ (Systems IIIB) causing the density to increase to $\rho \approx 1.0$ at the lower temperature. We then deform the nanopillars at a true strain rate of $\dot{\epsilon}_{\text{G}} = 10^{-4}$. We repeat this procedure for 50 replicas. We output monomer positions every 10,000 timesteps.

Softness Training using Support Vector Machine. We train the softness field for Systems II and III as in refs. 27 and 28. For System III, we analyze the time-averaged monomer positions during these trajectories, averaging every 5 timesteps in the 500 timesteps before each frame. We first extract a set of rearranging and nonrearranging particles from the early stage of the deformation (preshear band formation). To differentiate between these groups, we calculate a D^2_{min} field (19) in which we take the strain between frames to be commensurate with the amount of strain for a particle to complete a rearrangement ($\epsilon_G \approx 2.0 \times 10^{-3}$ for System II and $\epsilon_G \approx 6.6 \times 10^{-4}$ for System III) and take the cutoff radius ($R_c = 1.75$ d) to include the first shell of neighbors. We consider this field's local maxima and minima to be the rearranging and nonrearranging particles (29, 50). We next encode the local structure around these training examples as a high-dimensional vector, $\vec{G}$, of functions similar to the Behler–Perrinello (51) functions, which we describe in detail elsewhere (28, 52). Because large longitudinal strains cause significant changes in local density at later strains, we also consider these structural features scaled by deviations of the local packing density from the average density $(\rho - \langle\rho\rangle)/\langle\rho\rangle$. We append this scaled vector to the original vector to fully describe the local structure of our training examples, $\vec{G}^{\frown}\left((\rho - \langle\rho\rangle)/\langle\rho\rangle\vec{G}\right)$. We use these appended structural descriptors in $\mathbb{R}^{2N}$ as the input for a linear support vector machine (SVM) classification to calculate the hyperplane that best separates rearranging particles from nonrearranging particles. We compute softness as the signed distance from the hyperplane to the data points in the appended high-dimensional structural descriptor space. We exclude particles on the exterior of the pillars from training and testing for simplicity. We use the same softness field for both particle sizes in the granular raft experiment (System II) by rescaling by the average particle radius. To validate this model, we consider the probability of a particle being soft at a given D^2_{min} $P(S > 0|D^2_{\text{min}})$ for a set of pillars independent from the pillars that were used for training (see *SI Appendix*, Fig. S1 for test performance). This function has a strong monotonically increasing dependence on D^2_{min} that plateaus near 1, suggesting a strong correlation between softness and the size of plastic events.

Softness Training using a Neural Network. We train a 17-layer residual convolutional neural network to predict the local yield stress of each particle of System I. The architecture is similar to the "wide residual network" (53), except

for the following. First, the input is 128 × 128 grayscale (single channel) images, cropped from an image of the entire configuration, which has a resolution of 2048-by-2048 for configurations with $N = 10{,}000$ particles and 4096-by-4096 for configurations with $N = 64{,}000$ particles. One example of such an image is presented in *SI Appendix*, Fig. S2. Second, we used four groups of convolutions instead of three, since our input image is larger. Each group contains two ResNet blocks, as in ref. 53. Third, we used the "basic" version of ResNet blocks in figure 1 of ref. 53. While ref. 53 found that wider versions are better for image classification tasks, we find that they provide little improvement for our tasks. Fourth, we removed the last global-average pooling layer and softmax layer of the original neural network because they are only suitable for image classification tasks. These layers are replaced with a fully connected layer with a single neuron outputting a predicted local yield stress. Our loss function is the squared difference between the predicted and the actual local yield stress. We calculate the actual local yield stress using the procedure detailed in ref. 38. Last, we impose an L2 regularizer with regularization parameter 0.2 on all weights and biases of the neural network. We also augment the training data by randomly flipping it in both the horizontal and the vertical directions.

The neural network was trained on the configurations after equilibration at three different temperatures but before performing quasistatic shear. Both the training dataset and the test dataset are derived from five independent configurations with $N = 10{,}000$ particles equilibrated at $T_a = 0.025$, one configuration with $N = 64{,}000$ and $T_a = 0.1$, and one configuration with $N = 64{,}000$ and $T_a = 0.2$. For each configuration, we calculate the local yield stress of every particle using the protocol detailed in ref. 38 and asked the neural network to predict it. The neural network was trained in 40 epochs with batch size 16. We used Adam minimizer for training with a learning rate that decays exponentially from 3×10^{-4} to 3×10^{-6}. After training, the coefficient of determination on the test set is $R^2 = 0.5809$, i.e., 58.09% of the variance in the test data is captured by the prediction. Let the predicted local yield stress for a particle be Y_p; we then define softness as $S = \langle Y_p \rangle - Y_p$, where $\langle Y_p \rangle = 12.09$ is the average of Y_p at $T_a = 0.2$. Dividing Y by the shear modulus $G = 89$ gives the local yield strain. The initial value of the mean, $\langle S \rangle$, and the SD, σ_S, of the softness distribution for each system is shown in Fig. 1.

Data, Materials, and Software Availability. Simulation program data have been deposited in Github (54).

ACKNOWLEDGMENTS. We thank Misaki Ozawa and Ludovic Berthier for providing the initial soft-disk configurations used in this study. This work was supported by the NSF through grant MRSEC/DMR-1720530 (D.J.D., R.A.R., H.X., E.Y., G.Z.), and the Simons Foundation via the "Cracking the glass problem" collaboration #45945 (S.A.R., A.J.L.) and Investigator Award #327939 (A.J.L.). Also, the Flatiron Institute is a division of the Simons Foundation. This work used The Extreme Science and Engineering Discovery Environment (XSEDE) Stampede2 at the Texas Advanced Computing Center through allocation TG-DMR150034 (E.Y., R.J.S.I, R.A.R.), which is supported by NSF grant ACI-1548562.

Author affiliations: [a]Department of Physics, University of Pennsylvania, Philadelphia, PA 19104; [b]Chemical and Biological Engineering, Institute for Multiscale Simulation, Friedrich-Alexander-Universität Erlangen-Nürnberg, Erlangen 91058, Germany; [c]Department of Mechanical Engineering, University of Michigan, Ann Arbor, MI 48109; [d]Department of Physics, City University of Hong Kong, Hong Kong 999077, China; [e]Department of Chemical and Biomolecular Engineering, University of Pennsylvania, Philadelphia, PA 19104; [f]Materials Science and Engineering Division, National Institute of Standards and Technology, Gaithersburg, MD 20899; [g]Department of Physics, Emory University, Atlanta, GA 30322; and [h]Center for Computational Biology, Flatiron Institute, Simons Foundation, New York, NY 10010

1. E. D. Cubuk *et al.*, Structure-property relationships from universal signatures of plasticity in disordered solids. *Science* **358**, 1033–1037 (2017).
2. M. L. Falk, J. S. Langer, Deformation and failure of amorphous, solidlike materials. *Annu. Rev. Condens. Matter Phys.* **2**, 353–373 (2011).
3. A. Greer, Y. Cheng, E. Ma, Shear bands in metallic glasses. *Mater. Sci. Eng. R Rep* **74**, 71–132 (2013).
4. D. Bonn, M. M. Denn, L. Berthier, T. Divoux, S. Manneville, Yield stress materials in soft condensed matter. *Rev. Mod. Phys.* **89**, 035005 (2017).
5. A. Tanguy, Elasto-plastic behavior of amorphous materials: A brief review. *C. R. Phys.* **22**, 1–17 (2021).
6. M. Falk, Molecular-dynamics study of ductile and brittle fracture in model noncrystalline solids. *Phys. Rev. B* **60**, 7062 (1999).
7. O. Dauchot, S. Karmakar, I. Procaccia, J. Zylberg, Athermal brittle-to-ductile transition in amorphous solids. *Phys. Rev. E* **84**, 046105 (2011).
8. E. Y. Lin, R. A. Riggleman, Distinguishing failure modes in oligomeric polymer nanopillars. *Soft Matter* **15**, 6589–6595 (2019).
9. H. Xiao, R. J. Ivancic, D. J. Durian, Strain localization and failure of disordered particle rafts with tunable ductility during tensile deformation. *Soft Matter* **16**, 8226–8236 (2020).
10. S. Karmakar, E. Lerner, I. Procaccia, J. Zylberg, Effect of the interparticle potential on the yield stress of amorphous solids. *Phys. Rev. E* **83**, 046106 (2011).
11. M. Ozawa, L. Berthier, G. Biroli, A. Rosso, G. Tarjus, Random critical point separates brittle and ductile yielding transitions in amorphous materials. *Proc. Natl. Acad. Sci. U.S.A.* **115**, 6656–6661 (2018).
12. A. Shavit, R. A. Riggleman, Strain localization in glassy polymers under cylindrical confinement. *Phys. Chem. Chem. Phys.* **16**, 10301–10309 (2014).
13. K. Matsushige, S. Radcliffe, E. Baer, The pressure and temperature effects on brittle-to-ductile transition in PS and PMMA. *J. Appl. Polym. Sci.* **20**, 1853–1866 (1976).
14. K. Karimi, D. Amitrano, J. Weiss, From plastic flow to brittle fracture: Role of microscopic friction in amorphous solids. *Phys. Rev. E* **100**, 012908 (2019).
15. Z. Wang *et al.*, Stretchable materials of high toughness and low hysteresis. *Proc. Natl. Acad. Sci. U.S.A.* **116**, 5967–5972 (2019).
16. L. Zhang *et al.*, Using shape anisotropy to toughen disordered nanoparticle assemblies. *ACS Nano* **7**, 8043–8050 (2013).
17. P. Sollich, F. Lequeux, P. Hébraud, M. E. Cates, Rheology of soft glassy materials. *Phys. Rev. Lett.* **78**, 2020 (1997).
18. H. J. Barlow, J. O. Cochran, S. M. Fielding, Ductile and brittle yielding in thermal and athermal amorphous materials. *Phys. Rev. Lett.* **125**, 168003 (2020).
19. M. L. Falk, J. S. Langer, Dynamics of viscoplastic deformation in amorphous solids. *Phys. Rev. E* **57**, 7192 (1998).
20. A. R. Hinkle, C. H. Rycroft, M. D. Shields, M. L. Falk, Coarse graining atomistic simulations of plastically deforming amorphous solids. *Phys. Rev. E* **95**, 053001 (2017).
21. A. Nicolas, E. E. Ferrero, K. Martens, J. L. Barrat, Deformation and flow of amorphous solids: Insights from elastoplastic models. *Rev. Mod. Phys.* **90**, 045006 (2018).
22. M. Popović, T. W. de Geus, M. Wyart, Elastoplastic description of sudden failure in athermal amorphous materials during quasistatic loading. *Phys. Rev. E* **98**, 040901 (2018).
23. A. Barbot *et al.*, Local yield stress statistics in model amorphous solids. *Phys. Rev. E* **97**, 033001 (2018).
24. C. Liu, S. Dutta, P. Chaudhuri, K. Martens, Elastoplastic approach based on microscopic insights for the steady state and transient dynamics of sheared disordered solids. *Phys. Rev. Lett.* **126**, 138005 (2021).
25. D. F. Castellanos, S. Roux, S. Patinet, Insights from the quantitative calibration of an elasto-plastic model from a Lennard-Jones atomic glass. *C. R. Phys.* **22**, 1–28 (2021).
26. D. F. Castellanos, S. Roux, S. Patinet, History dependent plasticity of glass: A mapping between atomistic and elasto-plastic models. *Acta Mater*, 118405 (2022).
27. E. D. Cubuk *et al.*, Identifying structural flow defects in disordered solids using machine-learning methods. *Phys. Rev. Lett.* **114**, 108001 (2015).
28. S. S. Schoenholz, E. D. Cubuk, D. M. Sussman, E. Kaxiras, A. J. Liu, A structural approach to relaxation in glassy liquids. *Nat. Phys.* **12**, 469–472 (2016).
29. D. Richard *et al.*, Predicting plasticity in disordered solids from structural indicators. *Phys. Rev. Mater.* **4**, 113609 (2020).
30. V. Bapst *et al.*, Unveiling the predictive power of static structure in glassy systems. *Nat. Phys.* **16**, 448–454 (2020).
31. J. Paret, R. L. Jack, D. Coslovich, Assessing the structural heterogeneity of supercooled liquids through community inference. *J. Chem. Phys.* **152**, 144502 (2020).
32. E. Boattini, F. Smallenburg, L. Filion, Averaging local structure to predict the dynamic propensity in supercooled liquids. *Phys. Rev. Lett.* **127**, 088007 (2021).
33. Z. Fan, E. Ma, Predicting orientation-dependent plastic susceptibility from static structure in amorphous solids via deep learning. *Nat. Commun.* **12**, 1506 (2021).
34. F. Font-Clos *et al.*, Predicting the failure of two-dimensional silica glasses. *Nat. Commun.* **13**, 2820 (2022).
35. G. Jung, G. Biroli, L. Berthier, Predicting dynamic heterogeneity in glass-forming liquids by physics-informed machine learning. *Phys. Rev. Lett.* **130**, 238202 (2023).
36. E. Yang, R. A. Riggleman, Role of local structure in the enhanced dynamics of deformed glasses. *Phys. Rev. Lett.* **128**, 097801 (2022).
37. G. Zhang, S. A. Ridout, A. J. Liu, Interplay of rearrangements, strain, and local structure during avalanche propagation. *Phys. Rev. X* **11**, 041019 (2021).
38. G. Zhang *et al.*, Structuro-elasto-plasticity model for large deformation of disordered solids. *Phys. Rev. Res.* **4**, 043026 (2022).
39. R. J. S. Ivancic, R. A. Riggleman, Identifying structural signatures of shear banding in model polymer nanopillars. *Soft Matter* **15**, 4548–4561 (2019).
40. G. Picard, A. Ajdari, F. Lequeux, L. Bocquet, Elastic consequences of a single plastic event: A step towards the microscopic modeling of the flow of yield stress fluids. *Eur. Phys. J. E* **15**, 371–381 (2004).
41. Z. Budrikis, S. Zapperi, Avalanche localization and crossover scaling in amorphous plasticity. *Phys. Rev. E* **88**, 062403 (2013).
42. See supplemental material (URL will be inserted by publisher).
43. C. E. Maloney, A. Lemaitre, Amorphous systems in athermal, quasistatic shear. *Phys. Rev. E* **74**, 016118 (2006).

44. T. Albaret, A. Tanguy, F. Boioli, D. Rodney, Mapping between atomistic simulations and eshelby inclusions in the shear deformation of an amorphous silicon model. *Phys. Rev. E* **93**, 053002 (2016).
45. A. Barbot, M. Lerbinger, A. Lemaitre, D. Vandembroucq, S. Patinet, Rejuvenation and shear banding in model amorphous solids. *Phys. Rev. E* **101**, 033001 (2020).
46. L. Berthier, P. Charbonneau, A. Ninarello, M. Ozawa, S. Yaida, Zero-temperature glass transition in two dimensions. *Nat. Commun.* **10**, 1–7 (2019).
47. M. Singh, M. Ozawa, L. Berthier, Brittle yielding of amorphous solids at finite shear rates. *Phys. Rev. Mater.* **4**, 025603 (2020).
48. E. Yang *et al*., Understanding creep suppression mechanism in polymer nanocomposites through machine learning. arXiv [Preprint] (2022). http://arxiv.org/abs/2204.11996 (Accessed 9 May 2023).
49. M. Ozawa, L. Berthier, G. Biroli, G. Tarjus, Role of fluctuations in the yielding transition of two-dimensional glasses. *Phys. Rev. Res.* **2**, 023203 (2020).
50. S. A. Ridout, Ph.D. thesis (University of Pennsylvania, 2021).
51. J. Behler, M. Parrinello, Generalized neural-network representation of high-dimensional potential-energy surfaces. *Phys. Rev. Lett.* **98**, 146401 (2007).
52. E. Yang, R. J. Ivancic, E. Y. Lin, R. A. Riggleman, Effect of polymer-nanoparticle interaction on strain localization in polymer nanopillars. *Soft Matter* **16**, 8639–8646 (2020).
53. S. Zagoruyko, N. Komodakis, Wide residual networks. arXiv [Preprint] (2016). http://arxiv.org/abs/1605.07146 (Accessed 9 May 2023).
54. H. Xiaoa, Simulation programs for the structro-elasto-plastic models. source code for StEP simulations. https://github.com/OsCeZrCd/gridModel. Deposited 23 August 2023.